

A multiplatform code for the analysis of energy-dispersive X-ray fluorescence spectra

V.A. Solé^{a,*}, E. Papillon^a, M. Cotte^a, Ph. Walter^b, J. Susini^a

^a European Synchrotron Radiation Facility (ESRF), 6 rue Jules Horowitz B.P 220, 38043 Grenoble, France

^b Centre de Recherche et de Restauration des Musées de France, CNRS-UMR171, Louvre, 75041 Paris, France

Received 4 October 2006; accepted 6 December 2006

Available online 16 December 2006

Abstract

A user friendly program for X-ray fluorescence analysis has been developed at the European Synchrotron Radiation Facility. The program allows interactive as well as batch processing of large data sets and it is particularly well suited for X-ray imaging. Its implementation of a complete description of the *M* shell is particularly helpful for analysis of data collected at low energies. The code is platform independent (Linux, Windows, MacOS X, Solaris ...) and it is freely available for non-commercial use. Description of the algorithms used and practical examples are presented.

© 2006 Elsevier B.V. All rights reserved.

Keywords: X-ray fluorescence; X-ray imaging; Microfluorescence; Quantitative XRF analysis; Fundamental-parameters method

1. Introduction

Up to recent dates most, if not all, spectrum fitting for X-ray fluorescence (XRF) measurements at the European Synchrotron Radiation Facility (ESRF), namely beamlines ID13, ID18F, ID21 and ID22, had been performed using externally supplied commercial software mostly based on the AXIL package [1,2]. Whilst this software is fairly robust and reliable, we had very little influence over its development and, consequently, its direct integration into our control system and subsequent data analysis routines was not straightforward. A further limitation is such commercial software cannot be distributed to our user community.

A versatile non-linear least-squares fitting application had been already developed as part of the tools of the Beamline Instrumentation Software Support (BLISS) group at the ESRF. This fitting application, based on the Levenberg–Marquardt algorithm [3,4], is entirely implemented in Python, thus ensuring a high level of platform compatibility and a straightforward integration into the ESRF control system. The

logical next step was to write a dedicated function to describe the X-ray fluorescence spectra and feed that function into the fitting module.

The setup of the configuration parameters of the fit had to be as simple as possible. This practical requirement led to the development of a complete visualization and data analysis tool named PyMCA (Python multichannel analyzer). This application relies on the Python bindings to the C++ programming toolkit Qt [5] and the library Qwt [6] to build its platform independent graphical interface and plotting routines. Nevertheless, the fitting code can run in prompt or batch mode fully independent of any graphical package.

2. Algorithms

PyMCA follows several of the recipes given by Van Espen and Janssens in their excellent introduction to X-ray spectra evaluation [7].

2.1. Continuum/background Models

The continuum is modeled in two possible ways: estimation or fitting. In the former, the estimated background is subtracted from the experimental data prior to the least-squares fitting of

* Corresponding author. Tel.: +33 4 76 88 25 84; fax: +33 4 76 88 24 48.
E-mail address: sole@esrf.fr (V.A. Solé).

the fluorescence peaks. In the fitting mode the continuum is described by an analytical function which enters into the least-squares fitting algorithm. PyMCA implements both models.

Background can be estimated thru an iterative procedure in which the content of each channel is compared against the average of the content of its neighbours at a distance of i channels. If the content is above the average, it is replaced by the average. In order to speed up the procedure, i can be taken as a fraction of the peaks full-width-half-maximum (FWHM) at the beginning of the iterative process, being one at the end of it. An optional Savitsky–Golay smoothing at the beginning of the process is possible as recommended in [7].

The analytical functions currently supported to describe the background are polynomials of user selectable degree on $x=(E-E_{\text{mean}})$ or on $x=\exp(E-E_{\text{mean}})$ where E is the energy of the considered point of the spectrum and E_{mean} is the energy at the center of the fitting region.

2.2. Peak shape model

The response function of most solid-state detectors is predominantly Gaussian. In certain instances it may be necessary to resort to more complicated models such as Voigt or Hypermet [8] functions.

A Gaussian peak is characterized by three parameters: the position, width, and height or area. It is desirable to describe the peak in terms of its area rather than its height because the area is directly related to the number of X-ray photons detected, while the height depends on the spectrometer resolution. The first approximation to the profile of a single peak is then given by:

$$\frac{A}{s\sqrt{2\pi}} \exp\left[-\frac{(x_i-x_0)^2}{2s^2}\right] \quad (1)$$

where A is the peak area (counts), s the width of the Gaussian expressed in channels and x_0 the location of the peak maximum. The FWHM is related to s by $\text{FWHM}=2.3548 s$.

In Eq. (1) the peak area is a linear parameter; the width and position are non-linear parameters. This implies that a non-linear least-squares procedure is required to find optimum values for the latter two parameters. Linear least-squares fitting methods can be used assuming the position and width of the peak are known with high accuracy from calibration. Our code offers the possibility to perform either a non-linear fit or a linear fit by fixing all non-linear parameters to their initial values.

To describe part of a measured spectrum, the fitting function must contain a number of such functions, at least one for each peak. For 10 elements and 2 peaks ($K\alpha$ and $K\beta$) per element we would need to optimize 60 parameters. It is highly unlikely that such a non-linear least-squares fit will terminate successfully at the global minimum. To overcome this problem the fitting function can be written in a different way as shown in the next paragraphs.

2.3. FWHM and position of peaks

The first step is to abandon the idea of optimizing the peak position of all peaks independently. The energies of the X-ray fluorescence lines are typically known with an accuracy of 1 eV or better. The pattern of peaks observed in the spectrum is directly related to the elements present in the sample.

Based on these elements we can predict all of the X-ray lines that constitute the spectrum and their energies. The peak fitting function is therefore written in terms of energy rather than channel number.

Defining ZERO as the energy of channel 0 and expressing the spectrum GAIN in eV/channel, the energy of channel i is given by:

$$E(i) = \text{ZERO} + \text{GAIN} \times i \quad (2)$$

and the normalized Gaussian peak can be written as:

$$G(i, E_j) = \frac{\text{GAIN}}{s\sqrt{2\pi}} \exp\left[-\frac{(E_j-E(i))^2}{2s^2}\right] \quad (3)$$

with E_j the energy (in eV) of the X-ray line and s the peak width given by:

$$s^2 = \left(\frac{\text{NOISE}}{2.3548}\right)^2 + 3.85 \times \text{FANO} \times E_j \quad (4)$$

In this equation NOISE is the electronic contribution to the peak width (typical 80–100 eV FWHM), FANO is the Fano factor (~ 0.114 for silicon) and 3.85 the energy required to produce an electron-hole pair in silicon.

The non-linear least-squares fit optimizes ZERO, GAIN, NOISE and FANO for the entire fitting region, thus for all peaks simultaneously. The actual position and width of the peaks are calculated using the expressions (2) and (4).

2.4. Element line groups

A further simplification that can be applied to reduce the number of fitting parameters is to model entire elements rather than single peaks. Some lines can be considered as being grouped together such as the $K\alpha_1$, $K\alpha_2$ doublets or even all K lines of an element. A single area parameter A representing the total number of counts in the line group can then be fitted.

The spectrum of an element can then be represented by:

$$y_p(i) = A \sum_{j=1}^{N_p} R_j G(i, E_j) \quad (5)$$

where G are the Gaussians (or Hypermetts) for the various lines of E_j energy and R_j the relative intensities of the lines. The summation runs over all lines in the group (N_p) with $\sum R_j=1$. The program default threshold to consider two transitions as two terms in (5) is 10 eV. Below that, the two transitions are represented by a single line at an energy given by the weighted mean of both transition energies and a relative intensity given by the sum of the relative intensities of each transition.

2.4.1. K shell and L sub-shells

The transition probabilities of all lines originating from a vacancy in the same (sub-) shell (K , L_1 , L_2 ...) are constant, independent of the excitation. However, the relative intensities depend on the absorption in the sample and in the detector windows. To take this into account, the X-ray attenuation must be included in Eq. (5). The relative intensity ratios are obtained by multiplying the transition probabilities with an absorption correction term:

$$R_j' = \frac{R_j T_A(E_j)[1-T_D(E_j)]}{\sum_j R_j T_A(E_j)[1-T_D(E_j)]} \quad (6)$$

The absorption correction term $T_A(E)$, used in the Eq. (6) includes the X-ray attenuation in all layers and windows between the sample surface and the active area of the detector while the term $[1-T_D(E)]$ accounts for the possibility for the photon to go thru the detector without interacting.

If a sample composition is given, the program uses a parallel beam approximation taking $R_j'' = R_j' / \sum_j R_j'$ with

$$R_j' = \frac{\omega_j P_j(E_0) R_j T_A(E_j)[1-T_D(E_j)]}{\mu_T(E_0) + \mu_T(E_j) \frac{\sin\psi_1}{\sin\psi_2}} \times \left[1 - \exp \left\{ \left[\left(\frac{\mu_T(E_0)}{\sin\psi_1} \right) + \left(\frac{\mu_T(E_j)}{\sin\psi_2} \right) \right] \rho d \right\} \right] \quad (7)$$

where ω_j is the fluorescence yield of the considered shell, P_j takes into account the possibility to have a vacancy in the j shell, μ_T is the total mass attenuation coefficient of the sample, E_0 is the incident photon beam energy, ψ_1 and ψ_2 are the angles of the incoming and fluorescent beam respect to the sample surface, ρ is the sample density and d is the sample thickness.

2.4.2. L shell group

In order to obtain physically meaningful results, it is very often desirable to fit all L lines together. It is very common to express the term P_j in Eq. (7) as function of the considered element L shell jump ratios, Coster–Kronig transitions and total photoelectric mass attenuation coefficient of the considered element. This makes the implicit assumption that the relative intensities of the different L shell lines are independent of the incident energy except because of attenuation terms. However, this jump approximation is incorrect [9].

Given an initial photon energy, an initial weight is associated to each L_i sub-shell. This weight is calculated from the probability to create an initial vacancy on the respective L_i sub-shell after L shell photoelectric effect. Instead of expressing it in terms of the jump ratios, this probability can be expressed as the L_i photo-ionization cross section at the incident energy normalized to the total L shell photo-ionization cross section. The needed data were calculated by J.H. Scofield [10] and can be obtained from the RTAB database of Kissel [11].

Since the initial vacancy can be shifted to higher L_i sub-shells thru Coster–Kronig transitions, those initial weights lead to

$$\begin{aligned} P_{L_1} &= \sigma_{L_1}(E_0) \\ P_{L_2} &= \sigma_{L_2}(E_0) + f_{12}P_{L_1} \\ P_{L_3} &= \sigma_{L_3}(E_0) + f_{23}P_{L_2} + f_{13}P_{L_1} \end{aligned} \quad (8)$$

where σ_i is the L_i photo-ionization cross section at the incident energy and f_{ij} are the Coster–Kronig transition probabilities.

From Eqs. (7) and (8) it can be observed that $P_j(E_0)$ is the j sub-shell vacancy production cross section at the excitation energy. If the incident energy is above the element K shell binding energy, this cross section has to take into account vacancies originated from the transitions to the K shell. Radiative transitions to the K shell will originate additional vacancies in the L shell according to the K_α intensity ratios. $K-LL$ and $K-LX$ Auger transitions will also originate vacancies in the L shell. The needed non-radiative transition ratios can be found in [12]. PyMCA correctly implements the radiative branch of the de-excitation cascade. A correct implementation of the non-radiative branch would imply the use of X-ray emission probabilities in the presence of spectator vacancies. In the current implementation (program version 3.9.4), Auger transition ratios are neglected and radiationless transitions only considered as leading to equally distributed additional L shell vacancies. While this implementation of the de-excitation cascade is very crude, it is satisfactory because when the L X-ray energies are of practical interest, the radiative transitions to the K shell largely dominate against the Auger transitions to the same shell.

2.4.3. M shell group

The M shell group is treated analogously to Section 2.4.2 with the correction due to Coster–Kronig transitions given by

$$\begin{aligned} P_{M_1} &= \sigma_{M_1}(E_0) \\ P_{M_2} &= \sigma_{M_2}(E_0) + f_{12}P_{M_1} \\ P_{M_3} &= \sigma_{M_3}(E_0) + f_{23}P_{M_2} + f_{13}P_{M_1} \\ P_{M_4} &= \sigma_{M_4}(E_0) + f_{34}P_{M_3} + f_{24}P_{M_2} + f_{14}P_{M_1} \\ P_{M_5} &= \sigma_{M_5}(E_0) + f_{45}P_{M_4} + f_{35}P_{M_3} + f_{25}P_{M_2} + f_{15}P_{M_1} \end{aligned} \quad (9)$$

If the excitation energy is above the element L_3 sub-shell binding energy, M shell vacancies due to the de-excitation cascade have to be taken into account. As in the case of the L shell, the radiative transitions to the K and L shells are correctly considered. The non-radiative transitions are approximated taking average M -sub-shell vacancy distributions deduced from [12].

2.5. Sum and escape peaks

The escape fraction f is defined as the number of counts in the escape peak N_e divided by the number of detected counts (escape plus parent). PyMCA assumes normal incidence to the detector and considers escape only from the front surface. The

formulae used are derived from the work of Reed and Ware [13].

The area of the escape peak, relative to the area of the parent peak can be calculated from the escape fraction:

$$\eta = \frac{N_e}{N_p} = \frac{f}{1-f} \quad (10)$$

For a Si detector, the escape peaks can be modeled by a Gaussian at energy 1.742 keV below the parent peak. Including the escape peaks, the description of the fluorescence of element becomes

$$y_p(i) = A \sum_{j=1}^{N_p} R_j' [G(i, E_j) + \eta G(i, E_j - E_{\text{esc}})] \quad (11)$$

where G represents the Gaussian fitting function and E_{esc} the energy of the escaped photon.

So escape peaks are not fitted as truly independent peaks, but they are part of the multiplet. For spectra obtained with a Ge detector one needs to account in a similar way for both the Ge- $K\alpha$ and the Ge- $K\beta$ escape peaks for energies above the Ge K shell electron binding energy. For each E_j , PyMCA calculates all the detector fluorescent lines that can be originated and applies the formulae in [13] to each of them. This implementation automatically takes into account L shell escape lines. In order to limit the number of escape lines, the user can specify the maximum number of individual escape lines per E_j to be considered.

Summing correction is performed using a very intuitive approach. Since any of the peaks can be detected simultaneously with any of the other peaks, one can calculate the summing contribution of channel i , simply shifting the whole calculated spectrum by i channels and multiplying it by the calculated content of the channel times a fitted parameter. This is then repeated for all the points of the spectrum. The physical meaning of that parameter, for a time acquisition of 1 s, could be interpreted as the minimum time, measured in seconds, needed by the acquisition system to distinguish two photons individually and not consider them as a single photon.

2.6. Polychromatic sources

The above formulae had to be adapted to the case of an incoming beam presenting a set of discrete energies in order to account for harmonic contamination. The approach can also be applied to polychromatic sources, as X-ray tubes, provided they are modeled by a set of discrete energies.

Considering the excitation beam as composed of photons of energies E_{0k} with a relative rate w_k , we can generalize Eq. (7) as

$$R_j' = \sum_k \frac{w_k T_A(E_{0k}) \omega_j P_j(E_{0k}) R_j T_A(E_j) [1 - T_D(E_j)]}{\mu_T(E_{0k}) + \mu_T(E_j) \frac{\sin\psi_1}{\sin\psi_2}} \times \left[1 - \exp \left\{ \left[\left(\frac{\mu_T(E_{0k})}{\sin\psi_1} \right) + \left(\frac{\mu_T(E_j)}{\sin\psi_2} \right) \right] \rho d \right\} \right] \quad (12)$$

where the dependency on the incident photon energies has been explicitly shown. The term $T_A(E_{0k})$ has been introduced in

order to show that the program takes into account the different attenuation of the incoming photons in their path to the sample. The other equations remain valid provided E_0 is replaced by E_{0k} .

3. Data input and output

The program can read several common formats such as QXAS, AmpTek and multicolumn ASCII besides the specific ESRF data formats.

The output is generated as tabulated ASCII data for an easy export to dedicated plotting programs and as HTML for easy visualization. The end users can run a batch to analyze the data and browse the results with their favorite web browser.

4. Theoretical database

The program uses by default a built-in database in which, instead of using emission energies, it derives the emission energies from the binding energies of Larkins [14].

The K shell fluorescence yields are taken from Bambynek's formula [15] which is in very good agreement with [16]. The K shell radiative emission probabilities are taken from Scofield's Dirac-Fock calculations [17].

The L shell fluorescence yields and Coster-Kronig data are taken from [18]. The L shell radiative transition probabilities are from Scofield's Dirac-Hartree-Slater (DHS) work [19].

The M shell fluorescence yields and Coster-Kronig data are taken from Refs. [20,21] while the radiative emission probabilities are from Ref. [22].

For elements where theoretical data are missing, the needed values are calculated by interpolation.

Since a systematic comparison of the different theoretical data available was beyond our goals, the program supplies alternative and ready to be used files implementing K shell transition probabilities derived from Scofield's DHS work [19] and the L shell transition probabilities of Campbell [23] derived combining the Dirac-Fock [24] and the DHS [19] calculations of Scofield. In addition, the program exposes its database to the user as easy to edit ASCII files.

The L_1 fluorescence yields ω_{L_1} deserve to be considered in more detail. Campbell [25] gives a set of recommended ω_{L_1} showing variations of more than 50% respect to theoretical DHS data for some elements. We observe large differences between the calculated concentrations of lead containing samples when taking the lead L lines as a group and the concentrations calculated from the L_1 , L_2 and L_3 lines separately. While the concentrations obtained from the L , L_2 and L_3 lines are in good agreement, the concentration derived from the L_1 lines is much higher. This discrepancy can be solved by increasing ω_{L_1} respect to the theoretical value. In the case of lead, Campbell recommends a value 7% higher than the theoretical value while the experimental values of Werner et al. [26], obtained using monochromatic synchrotron radiation as excitation source, indicate a much higher value. For the time being (version 3.9.4) these corrections, although being necessary for a proper description of several L shell groups of lines, are not implemented and they are left to the user.

Mass attenuation coefficients are log–log interpolated into ASCII tables previously generated by XCOM [27].

5. Imaging

The ESRF fluorescence microscopy beamline ID21 performs imaging experiments at low excitation energies (less than 7.2 keV). Samples are scanned in steps down to 0.1 μm and X-ray fluorescence spectra are collected for typical acquisition times of 0.3 to 1 s per step. Online single element imaging is performed setting regions of interest (ROI) around the characteristic element peaks. This technique is fast and simple. However, in presence of heavily overlapping peaks, it is impossible to separate the different element contributions to the spectrum in this way. In such cases, it is necessary to fit all spectra separately and reconstruct an image from the fitted areas.

Fig. 1 illustrates the program capabilities in the case of complex systems. The description of the different shells allows the deconvolution of overlapped multiplets. The chosen example is a fit of a cumulated fluorescence spectrum obtained from a fragment of a XVIth century painting. The analyses were performed to better identify the pigments used by the painter. By one hand there is a multiplet formed by the superposition of the K lines of sulfur and chlorine with the M lines of lead. The other multiplet is formed by the superposition of the calcium K lines and the antimony L lines.

Fitted maps (Fig. 2) of these elements revealed the presence of grains containing sulfur and antimony, surrounded by a matrix of lead. The fitted maps of calcium and antimony, obtained at a beam energy of 7.2 keV (Fig. 2A and B respectively), are completely different, without any overlapping, meaning that the fit enables a good distinction of the elements.

In order to estimate the accuracy of the software, the same area was analyzed at different excitation energies, either below or above the lead M_5 edge, but always above the sulfur K edge. Sulfur was then considered as a reference. Fig. 2C shows the fitted map of sulfur obtained at a beam energy of 2.495 keV, i.e. below the lead M_5 edge. In this way, the sulfur map can be obtained without any interference from lead. Fig. 2D and E

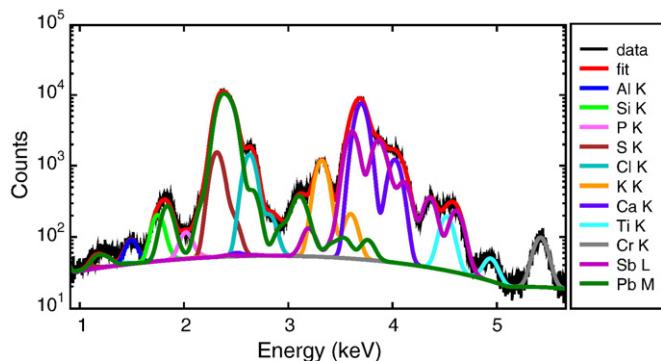


Fig. 1. Fit of the cumulated fluorescence spectrum of a fluorescence map of a XVIth-century painting fragment measured with a germanium detector. The broad peak at the lowest energy is mostly due to the escape of germanium L X-ray lines originated by lead M lines.

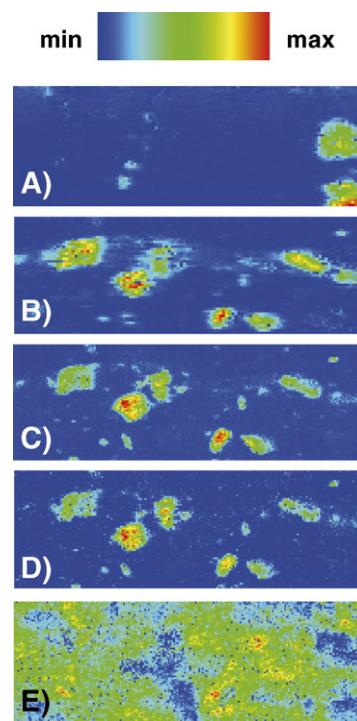


Fig. 2. Color-coded single-element distribution maps of a painting fragment containing sulfur, lead, calcium and antimony among others (see cumulated fluorescence signal, Fig. 1). Map size: $37 \times 21 \mu\text{m}^2$; step-size: 0.4 μm for A–B and 0.25 μm for C–E, in both directions. Beam energy: 7.2 keV for A and B; 2.495 keV for C; 2.55 keV for D and E. Each map was obtained via the program batch fitting. The maps correspond to calcium (A), antimony (B), sulfur (C and D), and lead (E). The color coding convention taken assigns blue to the minimum deconvoluted peak area and red to the maximum deconvoluted peak area of the element.

show fitted fluorescence maps acquired at 2.55 keV, i.e. above the lead M edges. They image the distribution of sulfur and lead respectively. The similarity of Fig. 2C and D proves the reliability of the fit, all over the map, despite the interfering presence of lead.

6. Quantitative analysis

The expected count rate of an element group of lines can be written as

$$A = I_0 C \frac{\Omega}{4\pi} \sum_j R_j'' \quad (13)$$

where I_0 is the incident beam rate, C is the mass fraction of the element in the sample and $\Omega/4\pi$ represents the detector geometric efficiency. Measured the areas A , the only unknown terms to calculate the mass concentrations are the incident photon flux and the detector efficiency. These parameters are given by the user either directly or indirectly asking the program to take one of the matrix elements as internal reference. Influence of secondary fluorescence excitation is neglected in all these calculations and should be estimated with standards or evaluated by Monte Carlo methods.

For multilayered samples the program considers the attenuation of the incoming and the outgoing beams thru the

different layers. With the current program implementation, if an element is present in several layers, the program cannot give the concentration of that element. It gives the concentration as if the entire signal would come from each layer in order to guide the scientist. With that information, users can proceed to estimate layer concentrations and/or thicknesses comparing the theoretical spectra of different sample matrices against the experimental data.

The analysis of spectra obtained with X-ray tubes was a feature soon requested by our users in order to profit from the built-in M shell description and from the implementation of the de-excitation cascade for the analysis of samples at their own labs. The formulae of Ebel [28] can be interactively used to generate an initial set of photon energies and weights that the user can refine with standards. The refinement procedure would consist on measuring a series of well characterized samples covering most of the tube spectral emission range. It is particularly convenient to use samples containing elements whose K shell can be excited by photons at the low energy side of the tube emission spectrum, as well as samples that can be excited at photon energies just above and just below the characteristic X-rays of the tube target. The weights and the total tube intensity I_0 have to be adjusted in order to match the theoretical and the fitted sample spectra. If the user knows the spectral distribution of his beam, he can skip this procedure and just enter his tube description.

7. Conclusion

PyMCA implements most of the needs of X-ray fluorescence spectroscopy. It has several unique features as the implementation of energy dependent photoelectric cross sections and a complete description of the M shell. It can process batches of thousands of spectra. It is portable (it already runs on Solaris, Linux, Windows and MacOS X) and it is freely distributed for non-commercial applications. Its open source policy makes it also a valuable fundamental-parameter research tool. The code can be downloaded from <http://www.esrf.fr/computing/bliss/downloads>.

References

- [1] P. Van Espen, H. Nullens, F. Adams, A computer analysis of X-ray fluorescence spectra, Nucl. Instrum. Methods Phys. Res., B Beam Interact. Mater. Atoms 142 (1977) 243–250.
- [2] B. Vekemans, K. Janssens, L. Vincze, F. Adams, P. Van Espen, Analysis of X-ray Spectra by Iterative Least Squares (AXIL): new developments, X-ray Spectrom. 23 (1994) 278–285.
- [3] K. Levenverg, A method for the solution of certain non-linear problems in least squares, Q. Appl. Math. 2 (1944) 164–168.
- [4] D.W. Marquardt, An algorithm for least-squares estimation of nonlinear parameters, J. Soc. Ind. Appl. Math. 11 (1963) 431–441.
- [5] Qt is available at <http://www.trolltech.com>. The Python binding PyQt is available from <http://www.riverbankcomputing.co.uk>.
- [6] Qwt is available at <http://sourceforge.net/projects/qwt>. The Python binding PyQwt is available from <http://sourceforge.net/projects/pyqwt>.
- [7] P.J.M. Van Espen, K.H.A. Janssens, Chapter 4: Spectrum Evaluation, in: R.E. Van Grieken, A.A. Markowicz (Eds.), Handbook of X-ray Spectrometry, Marcel Dekker, New York, 1993, pp. 181–293.
- [8] G.W. Phillips, K.W. Marlow, Automatic analysis of gamma-ray spectra from germanium detectors, Nucl. Instrum. Methods 137 (1976) 525–536.
- [9] A. Brunetti, M. Sánchez del Rio, B. Golosio, A. Simionovici, A. Somogyi, A library for X-ray matter interaction cross sections for X-ray fluorescence applications, Spectrochim. Acta Part B 59 (2004) 1725–1731.
- [10] J.H. Scofield, Theoretical Photoionization Cross Sections from 1 to 1500 keV, Lawrence Livermore Laboratory Report UCRL-51326, Livermore, Ca, 1973.
- [11] L. Kissel, Radiat. Phys. Chem. 59 (2000) 185–200 (RTAB database found at <http://www-phys.llnl.gov/Research/scattering/RTAB.html>).
- [12] M.H. Chen, B. Crasemann, Relativistic radiationless transition probabilities for atomic K - and L -shells, At. Data Nucl. Data Tables 24 (1979) 13–37.
- [13] S.J.B. Reed, N.G. Ware, Escape peaks and internal fluorescence in X-ray spectra recorded with lithium drifted silicon detectors, J. Phys. E 5 (1972) 582–584.
- [14] F.B. Larkins, Semiempirical Auger-electron energies for elements $10 \leq Z \leq 100$, At. Data Nucl. Data Tables 20 (1977) 311–387.
- [15] W. Bambynek, Proc. Conf. on X-ray and Inner Shell Processes in Atoms, Molecules and Solids, Aug. 20–24, Leipzig, Germany, 1984.
- [16] M.H. Chen, B. Crasemann, H. Mark, Relativistic K -shell Auger rates, level widths, and fluorescence yields, Phys. Rev., A 21 (1980) 436–441.
- [17] J.H. Scofield, Exchange corrections of K X-ray emission rates, Phys. Rev., A 9 (1974) 1041–1049.
- [18] M.H. Chen, B. Crasemann, H. Mark, Widths and fluorescence yields of atomic L -shell vacancy states, Phys. Rev., A 24 (1981) 177–182.
- [19] J.H. Scofield, Relativistic Hartree–Slater values for K and L X-ray emission rates, At. Data Nucl. Data Tables 14 (1974) 121–137.
- [20] M.H. Chen, B. Crasemann, H. Mark, Relativistic M -shell radiationless transitions, Phys. Rev., A 21 (1980) 449–453.
- [21] M.H. Chen, B. Crasemann, H. Mark, Radiationless transitions to atomic $M_{1,2,3}$ shells: results of relativistic theory, Phys. Rev., A 27 (1983) 2989–2994.
- [22] C.P. Bhalla, Radiative transition probabilities for vacancies in M subshells, J. Phys. B, Atom. Molec. Phys. 3 (1970) 916–924.
- [23] J.L. Campbell, J.-X. Wang, Interpolated Dirac–Fock values of L -subshell X-ray emission rates including overlap and exchange effects, At. Data Nucl. Data Tables 43 (1989) 281–291.
- [24] J.H. Scofield, Hartree–Fock values of L X-ray emission rates, Phys. Rev. A 10 (1974) 1507–1510; and (Erratum) Phys. Rev. A 12 (1975) 345.
- [25] J.L. Campbell, Fluorescence yields and Coster–Kronig probabilities for the atomic L subshells, At. Data Nucl. Data Tables 85 (2003) 291–315.
- [26] U. Werner, W. Jitschin, L -vacancy decay in heavy elements ($72 \leq Z \leq 82$) by the synchrotron photoionization method, Phys. Rev., A 38 (1988) 4009–4018.
- [27] M.J. Berger, J.H. Hubbell, XCOM: Photon cross sections on a personal computer. U.S. Department of Commerce, National Bureau of Standards NBSIR (1987) 87–3597.
- [28] H. Ebel, X-ray tube spectra, X-ray Spectrom. 28 (1999) 255–266.